10-10-2001

The Planetary Nebula A39: An Observational Benchmark for Numerical Modeling of Photoionized Plasmas

George H. Jacoby
Kitt Peak National Observatory

Gary J. Ferland
University of Kentucky, gary@uky.edu

Kirk T. Korista
Western Michigan University

The Planetary Nebula A39: An Observational Benchmark for Numerical Modeling of Photoionized Plasmas

Notes/Citation Information
Published in *The Astrophysical Journal*, v. 560, no. 1, p. 272-286.

Digital Object Identifier (DOI)
https://dx.doi.org/10.1086/322489

THE ASTROPHYSICAL JOURNAL, 560:272–286, 2001 October 10

THE PLANETARY NEBULA A39: AN OBSERVATIONAL BENCHMARK FOR NUMERICAL MODELING OF PHOTOIONIZED PLASMAS

GEORGE. H. JACOBY[1,2,3]
Kitt Peak National Observatory, P.O. Box 26732, Tucson, AZ 85726; jacoby@noao.edu
GARY. J. FERLAND[2]
Department of Physics and Astronomy, University of Kentucky, Lexington, KY 40506; gary@cloud9.pa.uky.edu
AND
KIRK T. KORISTA
Department of Physics, Western Michigan University, Kalamazoo, MI 49008; korista@wmich.edu
Received 2000 December 13; accepted 2001 June 12

ABSTRACT

Galactic nebulae are the main probes for the chemical evolution of the interstellar medium. Yet, recent observations have shown that chemical abundances determined from recombination and collisionally excited emission lines can differ by as much as an order of magnitude in some planetary nebulae (PNs). Many PNs have complex geometries and morphological evidence for interactions from stellar winds, and it is not clear to what extent winds, inhomogeneities, or shocked gas affect the observed spectrum. There currently is no full explanation for this discrepancy, which brings into question whether we understand the physical state of these low-density plasmas at all. This paper presents new spectroscopy from the KPNO Mayall 4 m telescope and imagery from the WIYN 3.5 m telescope of A39, a large PN with an exceptionally simple geometry. It appears to be a limb-brightened spherical shell, the simplest possible nebula. There is little evidence for external interactions, so this is the case in which photoionization simulations should be in near-perfect agreement with observation. We combine optical and UV spectroscopy to form a composite spectrum and compare this with photoionization models. No problems were encountered in reproducing the observed spectrum, although even this simple object has two distinct emission-line regions and exhibits several anomalies. A39 was too faint to detect the crucial heavy-element recombination lines in our data set, so it was not possible to compare collisional and recombination abundances. We predict the spectrum over a broad range of bandpasses to facilitate future observations that may probe deeper than our instrumentation allowed.

Subject headings: ISM: abundances — planetary nebulae: general — planetary nebulae: individual (Abell 39)

On-line material: machine-readable tables

1. INTRODUCTION

Nebulae (H II regions, planetary nebulae [PNs], and supernova remnants) are important probes of the end states of stellar evolution and of the chemical evolution of the universe (Pagel 1997). Serious discrepancies have been discovered between the abundances derived from collisional excitation and recombination lines (Liu 1998), which bring into question whether even the most basic physics is correct (Liu 1998). To some extent, the problems could be explained by temperature fluctuations (Mathis, Torres-Peimbert, & Peimbert 1998), but even these cannot account for the larger differences (Liu 1998; Garnett & Dinerstein 2001) and have the added burden of being physically implausible (Ferland 2001a).

Most nebulae display physical structure or inhomogeneities, and it is unclear whether these play a fundamental role in scrambling the observed spectrum (Williams 1992). In the usual case, inhomogeneities should not play a fundamental role in the observed spectrum since emission is dominated by the densest structures. It would take a "fine-tuning" of contributions of regions having various densities for the observed spectrum to be affected simultaneously by low- and high-density gas.

Thus, we are left with a fundamental dilemma: something is clearly incomplete in our understanding of these objects. It is not even clear whether this is a problem with the basic atomic data, whether we are overlooking the dominant physical processes that occur in the nebula, or whether this is simply due to complexity at the source.

This paper presents new imaging and spectroscopic observations and analysis of the PN A39. This object has an exceptionally simple appearance: it appears to be a one-dimensional projected shell. Since it is unlikely that the nebula has been strongly affected by winds or shocks, this seems to be the ideal object to establish as a benchmark for comparison with theoretical plasma emission codes.

Below we present new observations from the Kitt Peak 4 m Mayall telescope, WIYN 3.5 m telescope, and *Hubble Space Telescope* (*HST*) to create the needed database. Later sections compare these observations with the expected surface brightness of a thin shell and plane-parallel one-density photoionization models. While the object was too faint to observe the lines needed to test whether recombination and collisionally excited lines give the same abundances, we were able to develop a simple photoionization

[1] Current address: WIYN Observatory, P. O. Box 26732, Tucson, AZ 85726.

[2] Visiting Astronomer, Kitt Peak National Observatory, National Optical Astronomy Observatory, which is operated by the Association of Universities for Research in Astronomy (AURA), Inc., under cooperative agreement with the National Science Foundation.

[3] The WIYN Observatory is a joint facility of the University of Wisconsin-Madison, Indiana University, Yale University, and the National Optical Astronomy Observatory.

model to fit the spectrum. We also present the predicted spectrum, including faint lines, to guide later, deeper observations.

Still, a number of perplexing phenomena were uncovered, even in this very simple geometrical configuration, and where the spectral constraints are not overly tight. These are discussed in the last sections of the paper.

2. OBSERVATIONS

We had three principal goals for our observational program. (1) We wished to obtain deep images at high spatial resolution to check whether A39 is really a spherical shell with no significant knots or structures that would complicate the photoionization modeling. (2) We wished to obtain deep optical spectrophotometry in order to derive emission-line ratios of faint lines that will constrain the photoionization models. (3) We wished to extend the spectral constraints on the models by obtaining *HST* spectra in the UV for the bright nebular lines of carbon, helium, nitrogen, and oxygen. The latter observations are especially useful for determining the ionization structure of the nebula and the only way to measure carbon abundances with collisionally excited lines.

2.1. *Description of WIYN Imaging*

A39 was observed for us at the WIYN 3.5 m telescope on Kitt Peak on 1997 May 5 UT by D. Willmarth and on 1997 May 6 UT by D. Harmer, as a program in the "WIYN 2-Hour" queue. A series of four 15 minute exposures were taken in the light of [O III] λ5007 (filter FWHM = 45 Å). In addition, two 30 minute exposures were taken in the light of [N II] λ6583 (filter FWHM = 16 Å), as nebular structure is often emphasized in this line. With the S2KB 2048 × 2048 CCD, each 21 μm pixel subtends 0.″197 on the sky. The seeing for the combined image in [O III] was 0.″70, and the seeing in the combined [N II] image was 0.″56.

Figure 1 shows the average [O III] image, and Figure 2 shows the [N II] image after block averaging the image 3 × 3 to improve the visibility of the low surface brightness material. The [N II] line is so weak (see § 2.2) that the nebula is barely visible. Nevertheless, there is no evidence for any significant small-scale structure in either image.

We adopt the [O III] image (see Fig. 1) as the reference image from which the physical characteristics of the nebula are derived. In particular, we derive the diameter of the nebula and the position of the central star with respect to the cardinal points along the rim. We define the diameter as the maximum extent of the north-south and east-west chords, along the peaks of the rim. In the north-south direction, this diameter is 154.″5; in the east-west direction this diameter is 155.″1. We adopt the mean diameter of 154.″8 as the nebular diameter. Curiously, the central star is offset in position relative the intersection of the chords by $\sim$2″ to the west. If this were due to a nebular interaction with the interstellar medium (ISM), we would expect to see the nebula brightened along the rim to the west (Tweedy & Kwitter 1996), but the opposite is true. Furthermore, at the galactic height of 1420 pc (§ 3.4), A39 is not expected to encounter much of an ISM. We discuss an alternative explanation for the offset in § 3.

2.2. *Description of 4* m *Spectra*

A39 was observed with the Kitt Peak Mayall 4 m telescope and the RC Spectrograph on 1997 June 10, 11, and 12 UT. The spectrograph slit was oriented north-south and displaced 79″ to the east of the central star. The first two nights were devoted to the blue spectral region, from 3300 to 5500 Å, using grating BL181 in second order with a copper sulfate filter to block the first-order red light. On the first night, we used the atmospheric dispersion correction prisms to allow for accurate photometric calibrations down into the near-UV. The disadvantage of these prisms is that there is a significant loss of light below 4000 Å. Consequently, we removed the corrector on the second night in an attempt to measure the higher excitation lines in the near-UV (e.g., [Ne V]).

Note that the use of the atmospheric dispersion corrector prisms was not necessary for observations of this spectrally uniform extended object. For stellar sources, or objects having spatially varying spectra, the prisms are crucial. We became aware that the spectrum of A39 was not significantly varying on spatial scales of 1″–2″ after the first night, allowing us to remove the blue-light absorbing prisms and to probe into the near-UV. Having extended our data range to the region of [Ne V] λ3326, we saw evidence for this very high ionization species. Its presence, though, introduces several puzzles about this nebula, and high-ionization nebulae in general, that we will discuss further in § 6.

The third night was devoted to observations in the red spectral region, from 4750 to 9250 Å, again using grating BL181, but in first order and with a GG475 filter to block second-order blue light. For all three nights, we adopted a slit width of 1.″3, except that we opened the slit to 6″ when observing flux calibration standard stars HZ 44, BD +28°4211, Kopff 27, BD +25°3941, and Feige 110. However, as a result of clouds on the third night, the red calibration was restricted to HZ 44 alone.

In all, A39 was observed for 4 hr on night 1, for 6 hr on night 2, and for 3 hr on night 3 (in the red). The resolution in the blue was typically 3.5 Å, while in the red it was 6.3 Å. Seeing was typically 1.″1 each night, and the spatial scale along the slit was 0.″69 per pixel. The bright lines of Hβ and the [O III] $\lambda\lambda$4959, 5007 doublet provided the basis for tying the red spectrum to the blue.

The spectra were processed in the usual way, with wavelength calibrations based on arc lamps of helium, neon, and argon. Flat-fielding was based on a projector lamp to remove pixel-to-pixel nonuniformities, and twilight flats were used to remove variations along the slit. Flux calibration was achieved by referencing the spectra to the standard stars noted above.

Our slit position (see Fig. 1) was chosen to sample light from the luminous rim of A39, along 52″ of the eastern edge. We matched the offset of 79″ eastward from the central star to be consistent with the *HST* observations (see below). For our photoionization analysis, we averaged the spatially resolved spectra down to a single one-dimensional spectrum, thereby improving the detectability of lines as weak as 1% of Hβ to 10% accuracy. This average was based on the full extent of the visible line emission, which faded out quickly beyond the 52″ length but remained visible at a low surface brightness to nearly 95″. Consequently, we believe that there is an extended halo surrounding A39 with very low emission measure (see § 3).

The final blue and red spectra are shown in Figures 3–5, where Figure 4 provides a detailed view of the probable identification of the [Ne V] λ3326 line. The line ratios relative to Hβ are summarized in Table 1. For the blue spectra, the final ratios represent the average of the two nights,

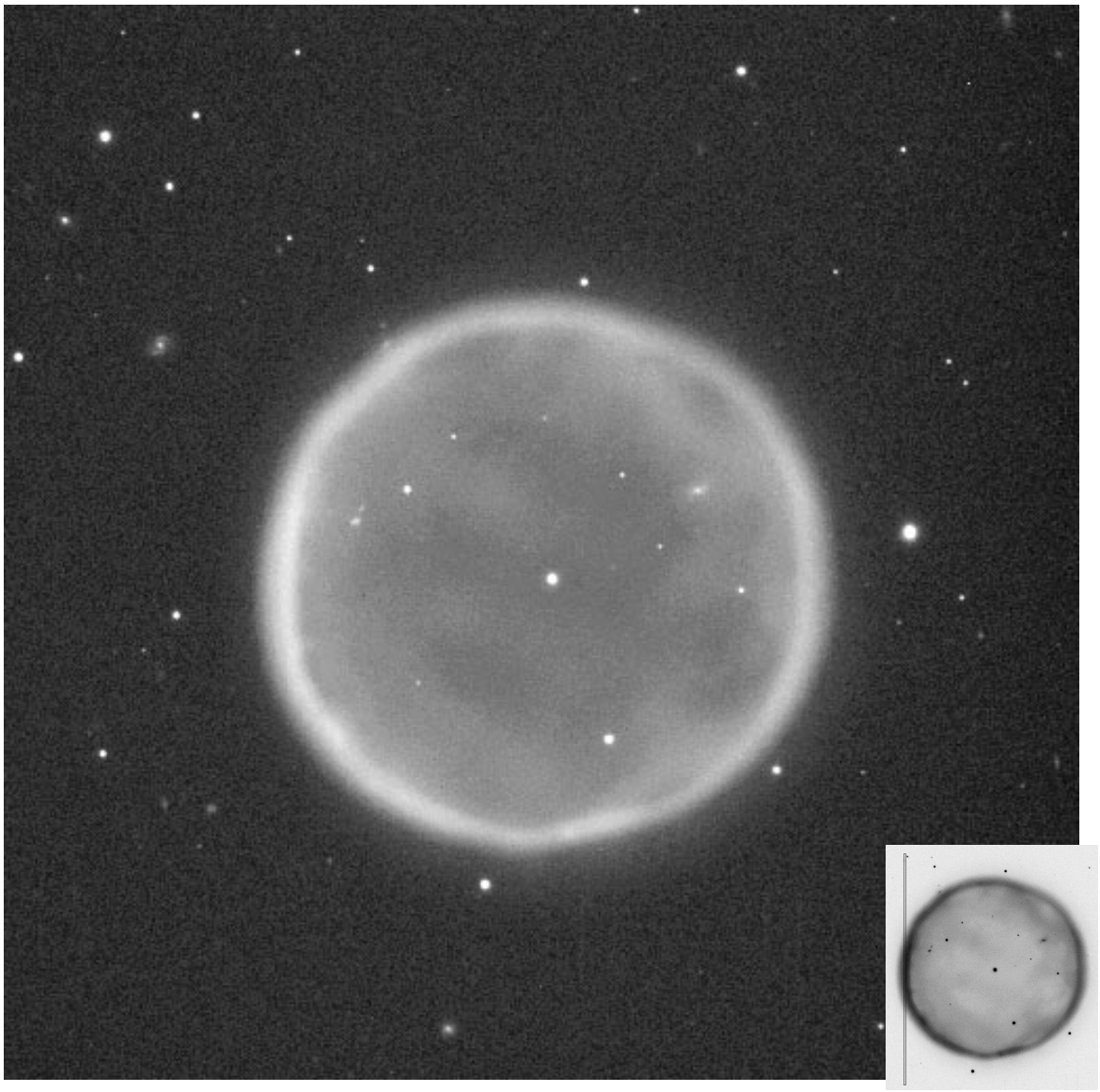

FIG. 1.—[O III] image of A39 taken with WIYN. North is up and east is to the left. The image is 335″ east-west and 328″ north-south. There is evident structure in the main body of the nebula, and so the assumption of a perfect spherical shell is incorrect at the detailed level. Also note that the east side of the nebula is about 50% brighter than the west side (see § 3). The inset shows the location of the spectrograph slit used for the 4 m. The *HST*/STIS slit length extends only across the bright part of the nebula and is nearly coincident with the 4 m slit placement.

which generally agreed extremely well, and rarely were the differences greater than 10%. Errors in the line strengths were estimated by measuring the rms uncertainty in the continuum near each line and then multiplying that value by the FWHM of the line. We then added in quadrature the standard deviation of multiple line measurements (e.g., 4686 was measured in each of the two blue spectra) and a systematic uncertainty of 2% from the flux calibration process.

2.3. *Description of HST Observations*

A39 was observed with the Space Telescope Imaging Spectrograph (STIS) on board *HST* in 1999 May, using the G140L and G230L gratings with the UV-MAMA detectors. The 26″ × 0.″2 slit (projected) was centered over the brightest portion of the eastern rim of the nebula, 79″ east of the central star, as indicated in the insert to Figure 1. At this position, the *HST* slit roughly spanned the inner chord of the bright eastern rim.

The 7700 s integration G140L spectrum when summed over the length of the slit revealed only two lines, He II λ1640 and the C IV λ1549 doublet blend, shown in Figure 6. These had measured fluxes of $5.2 \pm 0.5 \times 10^{-16}$ and $5.7 \pm 0.5 \times 10^{-16}$ ergs s^{-1} cm^{-2} integrated over the *HST* slit. Unfortunately, the 7500 s integration G230L spectrum was useless as a result of the large dark current noise permeating the G230L spectrum (the nebular surface brightness at these wavelengths was dimmer than had been expected). No emission lines were visible. Upper limits to the fluxes in N IV] λ1486, C III] λ1909, and Si III] λ1892 (including their forbidden line counterparts) were found to be 0.5, 9, and 9×10^{-16} ergs s^{-1} cm^{-2}, respectively.

2.4. *The Final Spectrum*

The 4 m and *HST* spectra were not precisely coincident, and the slit widths differed substantially, so these differences in aperture as well as seeing effects prevent us from directly

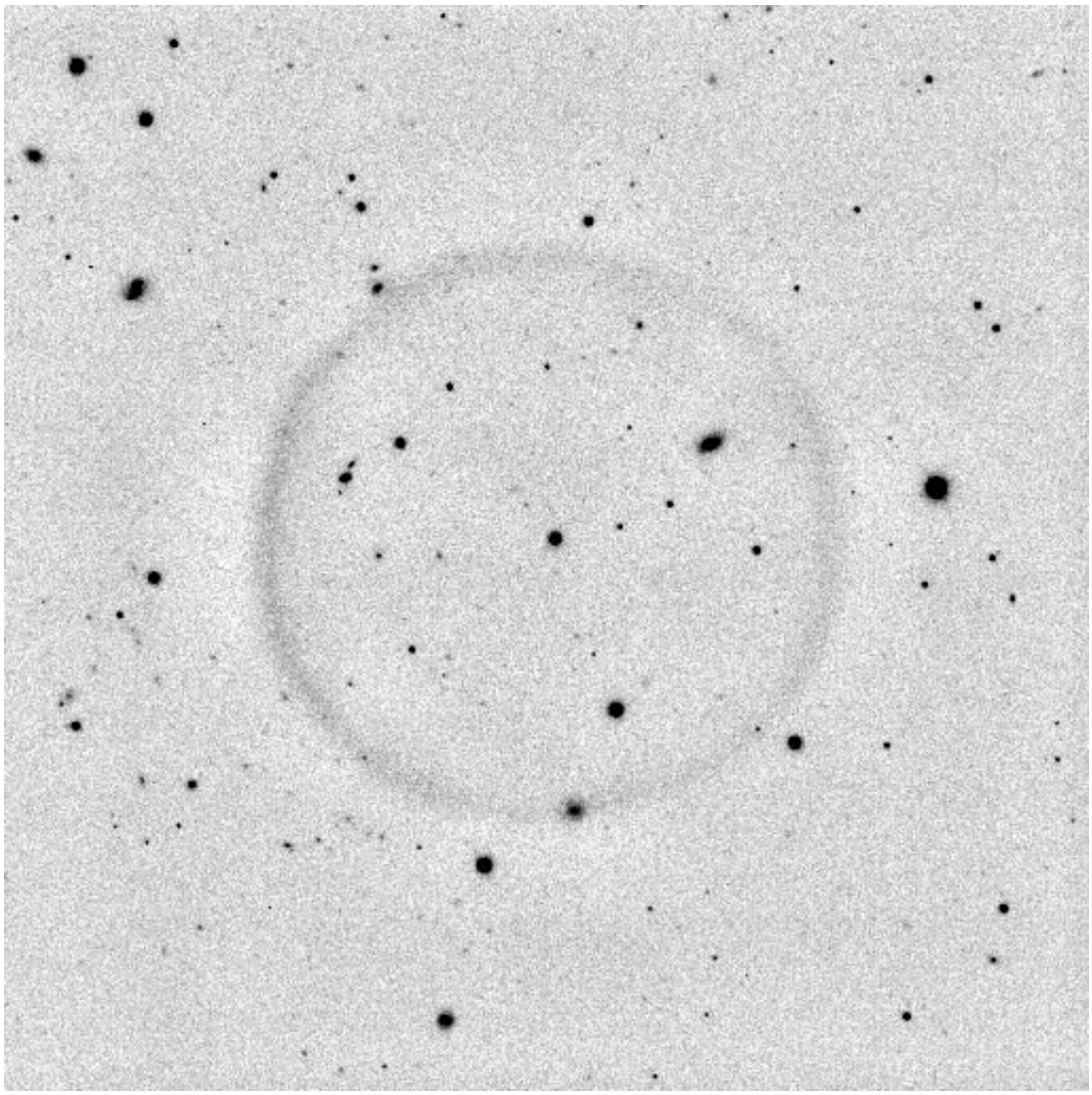

FIG. 2.—This [N II] image of A39 was taken with the WIYN 3.5 m telescope in 0.″56 seeing. This negative contrast image, blocked 3 × 3 to improve the detectability of faint structure, looks identical to the [O III] image with one exception: there is a very bright "knot" on the southern rim, almost due south of the central star. This could be a real knot in the nebula, but most likely it is a coincidence with a background galaxy, as there are numerous other galaxies of similar size and brightness in the field. (M. Bradshaw, an amateur astronomer who imaged A39 with a small telescope, pointed out the existence of this knot to G. H. J.)

comparing the optical and UV spectra. Thus, we assumed that the He II spectrum is close to case B at the temperature and density derived below. The numerical simulations presented later support this assumption. The expected 1640/4686 intensity ratio is then 6.97 (Storey & Hummer 1995). This value, the rescaled C IV intensity, and the upper limits to other UV lines have been entered into Table 1.

3. PROPERTIES OF THE PLANETARY NEBULA

This section describes the properties of the nebula, including its central star. These are summarized in Table 2. A basic premise to this study is that the nebula is a true spherical shell. Figure 7 shows the intensity distribution along an east-west cut through the center of the nebula based on an average of a 3″ swath. Overlaid on the data is a model distribution that assumes a perfect shell having a rim-to-rim diameter derived from the [O III] image and shell thickness of 10″. The model was then smoothed to match the observed 0.″7 seeing conditions of the data. We also tested models with shell thicknesses of 7″ and 13″, but these either overshot or undershot the rim surface brightness, respectively.

Deviations from the perfect shell model are minor until one moves well outside the peak in the rim of the shell. After that, the model seriously underestimates the true nebular surface brightness. We attribute this discrepancy to the presence of an extremely faint, low-density, highly ionized outer halo. We discuss this halo further in § 6.

3.1. *Size*

As discussed above, we measured the mean diameter of the nebula to be 154.″8 from the [O III] WIYN image, very nearly symmetric in the east-west and north-south directions. In a high contrast stretch of the nebular image, we see a faint halo that extends ~15″ beyond the rim. The spectral data, though, are more sensitive to low emission measure regions because the effective resolution (~3.5 Å) is far better at suppressing the background sky than an image through a

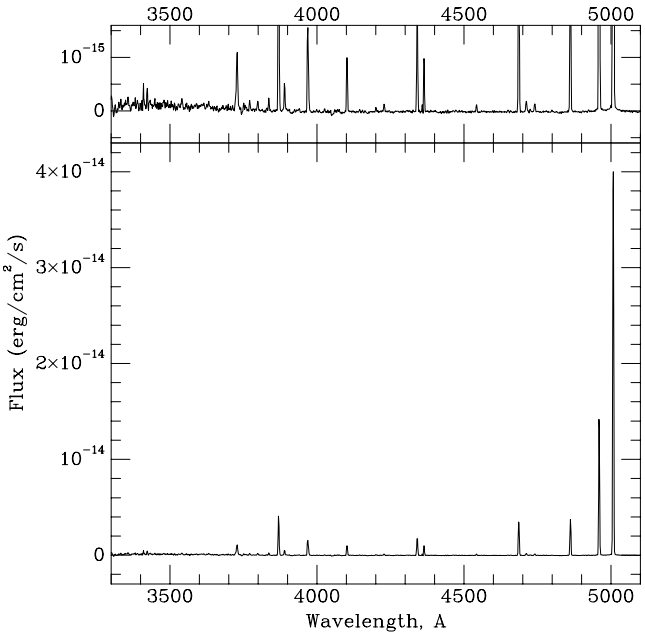

FIG. 3.—Blue spectral region of A39 observed on the second night of the Mayall 4 m spectroscopy run. The upper panel shows the spectrum expanded vertically to view the details of the weaker lines.

45 Å filter. When we plot the run of emission along the slit, having a spatial resolution of $\sim 1\farcs8$, we see emission as far across as 105″ along the slit. This corresponds to a radius of 95″ from the nebular center (18″ beyond the rim), or a diameter of 190″ assuming that the emission is symmetrically arranged about the nebula.

3.2. *Thickness of Shell*

Recall that we will be modeling A39 as a perfect spherical shell. For the purposes of the photoionization models, we need to define a shell thickness. We define the shell thickness as twice the half-width as measured from the peak of intensity in the rim moving outward along a radius vector. The shell thickness is not uniform around the nebula but is thickest along the east wall. Table 2 summarizes these measurements.

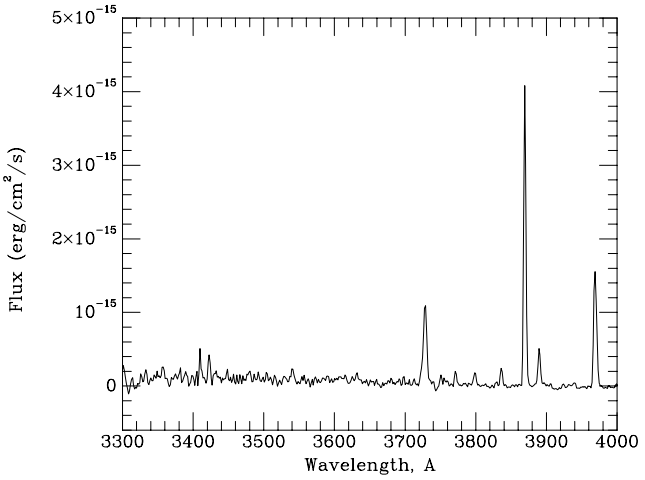

FIG. 4.—Expanded view of the region around the line of [Ne V] at 3426 Å. The line in question is the feature on the right of the pair just longward of 3400 Å.

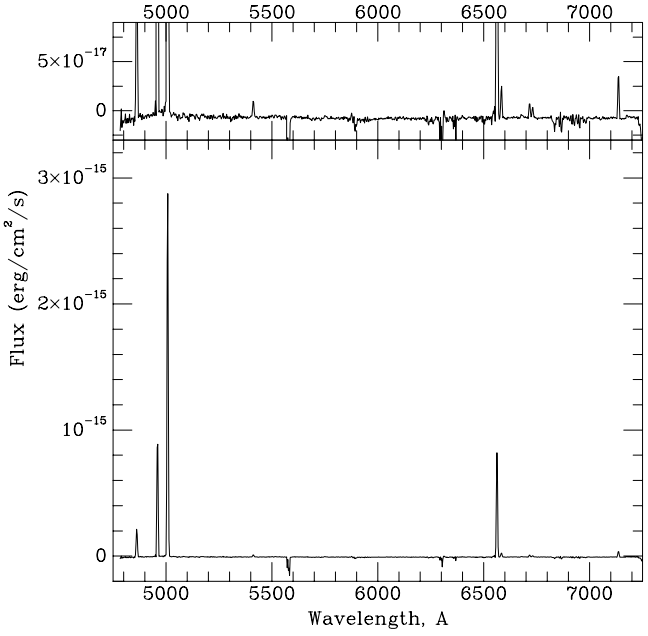

FIG. 5.—Red spectrum of A39 observed on the third night of the Mayall 4 m spectroscopy run. The upper panel shows the spectrum expanded vertically to view the details of the weaker lines. Data beyond 7200 Å are strongly affected by imperfect sky subtraction across the 95″ of the extracted spectrum and are not shown. Even over the limited spectral region, a number of poorly subtracted sky lines are evident (e.g., [O I] λ5577, Na D λ5890, [O I] λ6300).

We will assume a mean rim thickness of 10″.1 in subsequent sections.

3.3. *Reddening*

We refer to the reddening in terms of c, the logarithmic extinction at Hβ. We derive $c = 0.049 \pm 0.04$ from the observed Balmer decrement, Ha/Hβ, relative to the predicted value of 2.85 (Storey & Hummer 1995). This extinction is small and uncertain because of observational errors and the fact that the Balmer decrement predicted below is not precisely case B as a result of partial leakage of higher Lyman lines.

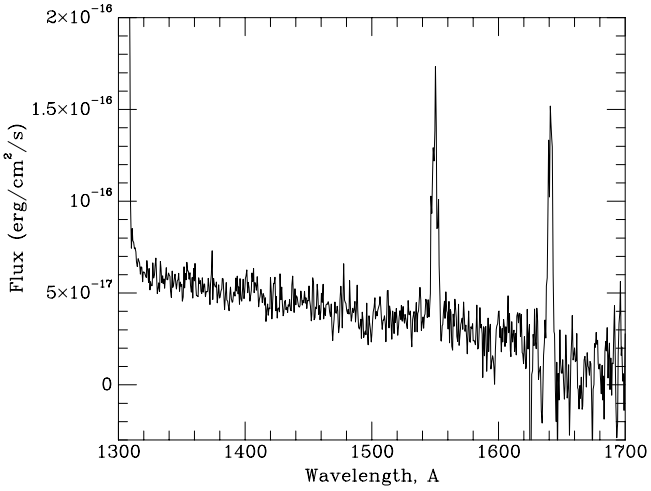

FIG. 6.—*HST*/STIS spectrum of A39, averaged along the full length of the projected 26″ slit. The only detected lines from the nebula are C IV λ1549 and He II λ1640.

TABLE 1

OBSERVED LINE AND CONTINUUM INTENSITIES

λ(obs)	Ion	λ(ion)	$I/H\beta$	$I/H\beta$ Corr	Error
	N IV]	1486	<0.6	<0.6	...
	C IV	1549	7.3	7.3	0.4
	He II	1640	6.62	6.62	Set
	Si III]	1892	<11	<11	...
	C III]	1909	<11	<11	...
Cont	νf_ν	3362	26.8	27.9	14.3
Cont	νf_ν	3496	24.7	24.7	10.4
Cont	νf_ν	3597	22.6	23.4	6.3
3422.6.....	[Ne V]	3426	0.070	0.098	0.014
3728.1.....	[O II]	3727	0.387	0.40	0.039
3771.4.....	H11 + He II	3771	0.042	0.043	0.007
3798.4.....	H10 + He II	3798	0.05	0.05	0.017
3835.8.....	H9 + He II	3835	0.06	0.06	0.002
3869.2.....	[Ne III]	3869	1.014	1.04	0.026
3889.5.....	H8 + He I	3889	0.14	0.14	0.014
3968.6.....	H7 + [Ne III]	3968	0.504	0.52	0.04
4026.7.....	He II	4026	0.019	0.019	0.007
4102.1.....	Hδ + He II	4101	0.267	0.273	0.014
4200.6.....	He II	4198	0.019	0.019	0.003
4227.9.....	[Fe V]	4227	0.035	0.036	0.001
4245.7.....			0.005	0.005	0.002
4340.8.....	Hγ + He II	4340	0.476	0.484	0.032
4363.8.....	[O III]	4363	0.234	0.238	0.019
4542.2.....	He II	4540	0.033	0.033	0.001
4578.6.....			0.007	0.007	0.003
4640.7.....	N III	4640	0.007	0.007	0.002
4657.9.....	[Fe III] + C IV		0.007	0.007	0.002
4686.2.....	He II	4686	0.95	0.956	0.031
4712.0.....	[Ar IV] + He II	4711	0.06	0.064	0.001
4725.5.....	[Ne IV]	4725	0.012	0.012	0.001
4740.5.....	[Ar IV]	4740	0.044	0.044	0.001
4861.7.....	Hβ + He II	4861	0.998	1.00	0.047
4861.7.....	Hβ	4861	0.95	0.95	0.047
4959.4.....	[O III]	4959	3.98	3.98	0.182
5007.3.....	[O III]	5007	11.34	11.31	0.524
5412.4.....	He II	5411	0.066	0.065	0.011
5876.9.....	He I	5876	0.019	0.019	0.008
6548.6.....	[N II]	6548	0.031	0.03	0.006
6562.8.....	Hα + He II	6563	2.959	2.859	0.06
6583.5.....	[N II]	6584	0.125	0.121	0.007
6716.8.....	[S II]	6716	0.059	0.057	0.003
6731.3.....	[S II]	6731	0.04	0.039	0.003
7134.9.....	[Ar III]	7135	0.06	0.058	0.004
9069.5.....	[S III]	9069	0.197	0.184	0.065

NOTE.—Table 1 is also available in machine-readable form in the electronic edition of the *Astrophysical Journal*.

A second estimate of c comes from the total H I column density in the line of sight past A39. Using Schlegel, Finkbeiner, & Davis (1998), we find an $E(B-V)$ of 0.06 corresponding to $c = 0.08$. This estimate is the total column through the galaxy and thus is an upper limit. Another estimate of the reddening can be derived from the color excess of the central star. The observed $B-V$ color is -0.33 (see § 3.7), and the limiting case for a hot star (Bergeron, Wesemael, & Beauchamp 1995) also yields $B-V = -0.33$, implying no reddening.

We adopt the value from the Balmer decrement, $c(H\beta) = 0.049$. The emission-line strengths in the fifth column of Table 1 have been corrected for this value using the reddening law of Cardelli, Clayton, & Mathis (1989), assuming a ratio of total to selective extinction of 3.1. Note that the line ratios in Table 1 (and subsequent tables) include a correction for the contribution of helium to the measured strength of the Balmer lines. In the case of A39, $I(H\beta)$ is reduced by 5% from its usual value of 1.00.

3.4. *Distance, Physical Dimensions, and Expansion Age*

Distance estimates for Galactic PNs are always problematic, and this case is no different. For typical estimates of the nebular properties (a mass of 0.2 $M_\odot$, a filling factor of unity, and $T_e = 10{,}000$ K) and an Hβ flux of 1.6×10^{-12} ergs cm^{-2} s^{-1} (Kaler 1983) corrected by $c = 0.049$, the Shklovskii method (see Pottasch 1984) gives a distance of 1.15 kpc. For an older nebula like A39, the shell is fully ionized and the shell mass could be much higher, possibly approaching 1 $M_\odot$ as suggested by Phillips & Pottasch (1984). If we adopt a mass of 0.6 $M_\odot$, a typical maximum value for a fully ionized nebula, a filling factor of 0.4 appro-

TABLE 2

ADOPTED NEBULAR PROPERTIES

Quantity	Value
Nebular diameter (arcsec)	154.8
East rim semithickness (arcsec)	5.97
West rim semithickness (arcsec)	5.67
North rim semithickness (arcsec)	4.83
South rim semithickness (arcsec)	3.74
Adopted mean semithickness (arcsec)	5.05
Adopted rim thickness (arcsec)	10.1
Radius (north) (arcsec)	77.6
Radius (south) (arcsec)	76.9
Radius (east) (arcsec)	79.3
Radius (west) (arcsec)	75.8
$c(\mathrm{H}\beta)$	0.049
Adopted distance (kpc)	2.1
Nebular Density (e^- cm^{-3})	30
Mass of nebula ($M_\odot$)	0.6
Mass of central star ($M_\odot$)	0.61

priate for the observed shell thickness (§ 3.2), and $T_e = 15{,}000$ K (see § 4.3), we then find a distance of 2.1 kpc, the value we adopt. We note in passing that McCarthy, Méndez, & Kudritzki (1997) derived a distance of 2 kpc based on an atmospheric model of the central star, thereby supporting the arguments for our adopted parameters.

At 2.1 kpc (6.5×10^{21} cm), the radius of the main shell (77.″4) corresponds to a physical radius of

$$R_{\rm shell} = 2.42 \times 10^{18} \Theta_{77} D_{21} \text{ cm} , \quad (1)$$

or 0.78 pc. Here Θ_{77} is the angular radius in units of 77″ and D_{21} is the distance in units of 2.1 kpc.

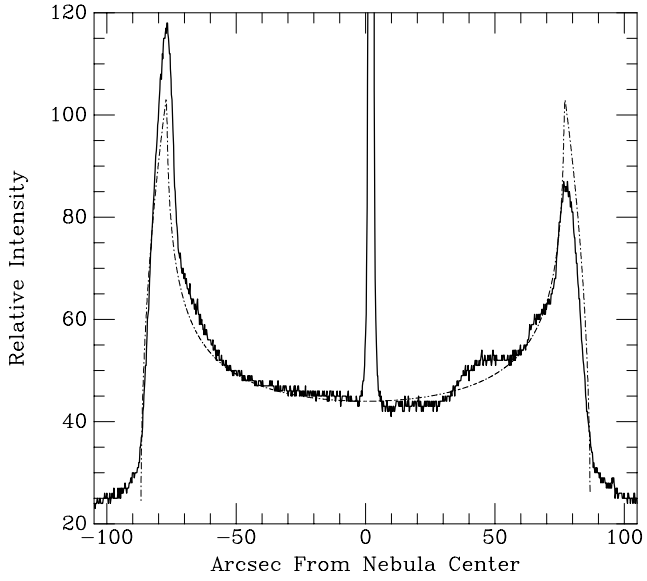

FIG. 7.—Radial distribution of A39 shown in this east-west diameter cut through the central star (*large spike near the middle*). A model spherical shell with a 10″ rim thickness was chosen to model the nebula (*smooth symmetric curve*). The model, after being smoothed to the 0.″7 seeing profile, matches the data profile fairly well, although it is too faint on the east side while being too bright on the west side. Models with 7″ or 13″ shell thicknesses are less successful at matching the data; the thinner shell produces brightness peaks that rise too high, and the thicker shell has the opposite result. In all cases, spherical shell models do not reproduce the faint extended halo; this apparently geometrically simple nebula offers a few complexities.

Hippelein & Weinberger (1990) found expansion velocities ranging between 32 and 37 km s^{-1}, depending on which ion they used. A velocity of 34 km s^{-1} corresponds to an expansion age of ~23,000 yr. For a free expansion, the ratio of the range in velocities to the expansion velocity (0.148) would also be the ratio of the shell thickness to the radius (0.131). The shell is slightly thinner than expected given the assumed distance and measured range in velocities.

The angular thickness of the shell (10.″1) at a distance of 2.1 kpc corresponds to a physical thickness of

$$\delta r_{\rm shell} = 3.17 \times 10^{17} \Theta_{10} D_{21} \text{ cm} ,$$

or 0.103 pc. Here Θ_{10} is the thickness in units of 10.″1.

At the distance of 2.1 kpc, the Galactic latitude of A39 (42.°5) implies a height above the Galactic plane of 1.42 kpc.

3.5. *Position of Central Star*

The central star is located off-center with respect to the ridgeline of the rim. The positional offsets are listed in Table 2. In summary, the star is ~2″ west of the nebular center. Within the measurement uncertainty, there is no significant north-south offset. At the adopted nebular distance of 2.1 kpc this offset corresponds to 0.020 pc, or 6.3×10^{11} km. For the adopted nebular age (§ 3.4) of 23,000 yr, this stellar offset requires a peculiar transverse velocity of only 0.9 km s^{-1}. We discuss a possible rationale for the offset in § 6.3.

3.6. Hβ *Surface Brightness, Luminosity, and Mean Intensity*

Kaler (1983) quotes an integrated Hβ flux of 1.6×10^{-12} ergs cm^{-2} s^{-1}. Correcting for an extinction of $c(\mathrm{H}\beta) = 0.049$ brings this up to 1.8×10^{-12} ergs cm^{-2} s^{-1}. For the distance of 2.1 kpc, the luminosity in Hβ is then

$$L(\mathrm{H}\beta) = 9.4 \times 10^{32} D_{21}^2 \text{ ergs s}^{-1} . \quad (2)$$

Taking the diameter as 154.″8 yields an average surface brightness in Hβ of

$$S(\mathrm{H}\beta) = 9.6 \times 10^{-17} \Theta_{77}^{-2} \text{ ergs arcsec}^{-2} \text{ s}^{-1} . \quad (3)$$

For isotropic emission this corresponds to a mean intensity of

$$4\pi J(\mathrm{H}\beta) = 5.1 \times 10^{-5} \Theta_{77}^{-2} \text{ ergs cm}^{-2} \text{ s}^{-1} . \quad (4)$$

3.7. *Stellar Properties*

Napiwotzki & Schönberner (1995) estimate the V magnitude for the central star of A39 as 15.6 ± 0.2 based on their spectrophotometry. This is similar to Abell's (1966) photoelectric measurements, which yielded $V = 15.60$ and $B-V = -0.33$, but much brighter than the values of $V = 16.39$ and $B-V = -0.83$ from Tylenda et al. (1991), also based on spectrophotometry. Kaler (1983) gives $V = 15.76$ and $B-V = -0.33$, but these are supposedly based on Abell's data. Given the nonphysical value for $B-V$ from the Tylenda paper (although the B magnitude of 15.56 is similar to the other measurements), we reject that V-band measurement and adopt an apparent V magnitude of 15.6. Correcting for reddening, we find $m_v = 15.5 \pm 0.2$.

Based on model atmospheres analyses, the stellar temperature and gravity were derived by Napiwotzki (1999) to be $T = 117{,}000 \pm 11{,}000$ K and $\log g = 6.28 \pm 0.22$. Similarly, McCarthy et al. (1997) find $T = 110{,}000$ K and $\log g = 6.3$. For the central star, Napitwotzki finds a helium

abundance corresponding to $N(\mathrm{He})/N(\mathrm{H}) = 0.14 \pm 0.03$. Adopting a central star temperature of 150,000 K implied by our best-fit models (§ 5) and the log g value above, the central star mass is 0.61 $M_\odot$. This is a fairly typical value and suggests that the progenitor star of A39 had an initial mass of $\sim$2.1 $M_\odot$. We base this estimate on the initial to final mass relation recommended by Weidemann (2000), combined with the open cluster studies of Claver et al. (2001) and the white dwarf measurements in the globular cluster M4 by Richer et al. (1997) to tie down the low-mass end. Had we adopted the smaller central star mass ($\sim$0.56 $M_\odot$) estimates from McCarthy et al. (1997) and Napiwotzki (1999) based on their atmospheric analyses that yield lower stellar temperatures, then the progenitor would have been about 1.3 $M_\odot$.

4. ANALYTICAL EMISSION-LINE ANALYSIS

4.1. *Electron Density and Shell Mass*

The observed ratio of the [S II] doublet, $\lambda\lambda$6716/6731 (1.48 ± 0.1), is consistent with the low-density limit but sets a limit of $n_e < 100$ cm^{-3} on the electron density. We do not have the spectral resolution to split the density-sensitive [O II] lines at $\lambda\lambda$3726, 3729.

The density can also be estimated from the surface brightness in a recombination line. We assume a plane-parallel geometry and the mean intensity of Hβ derived above (eq. [4]), $4\pi J(\mathrm{H}\beta) = 5.1 \times 10^{-5}$ ergs cm^{-2} s^{-1}. We assume that this emission is produced by a shell with twice the observed thickness (our line of sight passes through both sides of the shell), or $2r_{\mathrm{shell}} = \Theta_{10} D_{21}\, 6.33 \times 10^{17}$ cm. Assuming case B hydrogen emissivity at a temperature of 15,000 K (Storey & Hummer 1995),

$$4\pi j_B(\mathrm{H}\beta) = 8.60 \times 10^{-26} \text{ ergs cm}^3 \text{ s}^{-1}\,, \qquad (5)$$

then the density needed to produce the observed surface brightness is

$$n^2 = 4\pi J(\mathrm{H}\beta)/4\pi j_B(\mathrm{H}\beta)/2r_{\mathrm{shell}} = 934(\Theta_{10} D_{21})^{-1} \text{ cm}^{-6}\,, \qquad (6)$$

or $n \approx 30$ cm^{-3}. This density is consistent with the low-density limit suggested by the [S II] doublet and will be assumed in the following discussion.

The mass of gas in the shell derived with this density is given by

$$M_{\mathrm{shell}} = 4\pi R^2 \delta r n \mu = 2 \times 10^{33} D_{21}^3 \text{ g}\,, \qquad (7)$$

where the density and shell geometry outlined above were assumed and μ is the mean molecular weight of the gas. The shell mass is large, roughly 1 $M_\odot$.

Recall that we adopted the somewhat smaller mass of 0.6 $M_\odot$ in § 3.4 to derive a distance. This difference in masses may provide further evidence that the effective thickness of the nebula's shell is larger than indicated by the measurements in § 3.2, as initially evidenced by the extended luminosity distribution in Figure 7. Furthermore, because the high mass determined from equation (7) depends strongly on the uncertain distance estimate, we include this calculation only to illustrate that the different approaches to deriving nebular parameters are not grossly discrepant.

The hydrogen recombination timescale ($\approx 1/\alpha_A n$; $\alpha_A = 3.1 \times 10^{-13}$ cm^3 s^{-1}; Osterbrock 1989) for this density is $\sim$3400 yr, about 10 times shorter than the expansion age. The thermal timescale is even shorter: 600 yr. So, despite its low density, the atomic processes in this nebula are likely to have time to come to time-steady conditions.

4.2. *Electron Temperature*

The nebular electron temperature is set by the observed intensity ratio of the $\lambda\lambda$5007/4363 [O III] lines, 48 ± 4, and is in the range $\log T_e = 4.19 \pm 0.02$ ($14{,}800 < T_e < 16{,}000$ K). We adopt 15,400 K as a characteristic electron temperature. The temperature-sensitive [N II] λ5755 line is too faint to detect in this high-ionization nebula.

4.3. *Photoelectric Heating Rate*

The photoelectric heating rate for a typical PN ionizing radiation field (assuming a mean photoelectron energy of $\langle\varepsilon\rangle = \langle h\nu - 13.6\,\mathrm{eV}\rangle \approx 5$ eV) is

$$G = n^2 \alpha_B \langle\varepsilon\rangle \approx 2.3 \times 10^{-9} \text{ eV cm}^{-3} \text{ s}^{-1}\,, \qquad (8)$$

where we used the density and temperature deduced above. The heating rates due to galactic background cosmic rays, the Galactic diffuse ionizing radiation field, and the cosmic background are all much smaller and can be neglected. The nebula should be predominantly photoionized by the radiation field of the central star.

4.4. *Total Luminosity in Ionizing Photons*

The luminosity in Hβ (eq. [2]) corresponds to a total recombination rate within the nebula of

$$R_{\mathrm{recom}} = \frac{L(\mathrm{H}\beta)\alpha_B}{4\pi j_B(\mathrm{H}\beta)} \approx 2.0 \times 10^{45} D_{21}^2 \text{ s}^{-1}\,, \qquad (9)$$

where $\alpha_B = 1.84 \times 10^{-13}$ cm^3 s^{-1} is the case B recombination coefficient at the assumed temperature. This is equal to the total number of hydrogen-ionizing photons emitted by the central star if the nebula is radiation bounded and a lower limit to this number if the nebula is matter bounded. We have assumed that the covering factor W, the fraction of 4π sr covered by the nebula as seen from the central star, is unity, as suggested by the images.

At a distance of 2.1 kpc the extinction-corrected V magnitude corresponds to an absolute magnitude of $M_V = 3.9$. We expect the central star to have a temperature somewhat greater than 10^5 K. It is simple to show that the total number of hydrogen-ionizing photons emitted by the series of Rauch (1997) stellar continua, normalized to this visual magnitude, is far larger than the number of photons given by equation (9). We infer that the nebula only absorbs a small fraction of the incident continuum. This, together with the very weak low-ionization lines (i.e., weak [O II], [N II], and [S II], and no [O I]), suggests that the nebula is matter bounded. For this geometry, the gas is optically thin to the ionizing continuum and hydrogen is fully ionized across the cloud.

Stasinska, Gorny, & Tylenda (1997) used the Zanstra method to determine a stellar temperature of 36,000 K, clearly too small to account for the observed high-ionization spectrum. The Zanstra method fails with a too low temperature when the nebula is optically thin to ionizing radiation. This further strengthens the case that the cloud is matter bounded.

If we accept that the total recombination rate within the nebula is smaller than the total rate of ionizing photons

emitted by the central star [$Q(H)$] because the cloud is matter bounded, then we can estimate the optical depth of the shell in ionizing radiation. The Rauch atmospheres give $Q(H) \sim 10^{47}$–10^{48} s^{-1} for temperatures greater than 10^5 K and the absolute magnitude quoted above. We assume $Q(H) \sim 2 \times 10^{47}$ s^{-1}, appropriate for this magnitude and a temperature of 150,000 K. The optical depth in the Lyman continuum is then

$$\frac{R_{\rm recom}}{Q(H)} = [1 - \exp(-\tau_{\rm Lyman})] \cong \tau_{\rm Lyman} \approx 10^{-2} . \quad (10)$$

For thermal velocities the optical depth in Lyα is of order 10^4 times that in the Lyman continuum, so Lyα will have optical depths of roughly 100. This will be decreased even more if nonthermal line widths are present, as is suggested by the measured range of expansion velocities (Hippelein & Weinberger 1990). Depending on details, higher Lyman lines, which have smaller optical depths than Lyα, may well be optically thin. In this case the hydrogen emission spectrum goes over to case C conditions (Ferland 1999) rather than the case B assumed here. The emissivity and Balmer decrement are both altered in this situation, introducing an uncertainty in our mass and reddening estimates. All of the relevant physics is included in the numerical simulations presented below.

5. A PHOTOIONIZATION MODEL

A39 appears to be the ideal PN for a photoionization analysis because of its geometric simplicity. This was the original motivation for our study. This section outlines the steps taken in fitting the spectrum with a photoionization model.

Throughout this study, we use Version 96.00 of the spectral synthesis code CLOUDY (Ferland 2001b). The Rauch (1997) solar abundance stellar atmospheres were used. A surface gravity of $\log g = 6$ was assumed, as suggested by the papers by Napiwotzki and McCarthy (these actually suggest $\log g = 6.3$). Calculations (not presented here) showed that this lower surface gravity produced better results than $\log g = 8$ and that the solar abundance Rauch models produced better agreement than the halo (1/10 solar) abundance mix.

It is not meaningful to fit a spectrum with an accuracy greater than the fundamental uncertainties in the atomic data. Most rates and cross sections come from ab initio quantum theory. Most calculations of collision rates were done with the Belfast R-matrix codes and generally quote uncertainties of 15%. On average the database should be much better than this since errors should not be correlated. No one collisionally excited line can be predicted with an accuracy better than 15%, since the uncertainties enter in both the collision strength and transition probability. The situation for recombination lines of H I, He I, and He II is much better since their intensities depend mainly on the capture cascade processes. The theoretical predictions of their intensities should be accurate to 1%.

Heavy elements recombine predominantly by dielectronic recombination through low-lying autoionizing levels. Accurate rates are not known for most third-row ions since the positions of the autoionizing levels are not known (Nussbaumer & Storey 1987). Recent experimental measurements (Savin et al. 1999) show that theoretical estimates are often off by a factor of 2, and the scatter among theoretical rates is about this large (Savin 2000). This most critically affects the S III/S II and Ar IV/Ar III balance (Ali et al. 1991). Accordingly, fitting these ions will receive less weight in the following.

In the fitting process we have used the greater of the observational error or 15% in the uncertainty in collisionally excited lines and the observational error in the recombination lines. The strong [O III] λ5007 line is an exception: this must be fitted to high accuracy since it is a dominant coolant in the nebula; its intensity represents overall energy balance rather than the atomic physics.

5.1. *Constant Temperature Models*

As a first step CLOUDY was used in its optimization mode to fit the He I, He II, [O III], [O II], and [Ne III] spectra. This process is most efficient when the code starts near a solution and the minimum number of parameters is varied. At this stage the temperature of the central star was varied, along with the ionization parameter U and the abundances of O and Ne.

The initial set of calculations assumed a constant electron temperature of 15,400 K. The constant temperature assumption has two benefits. First the numerical simulation of a single cloud is nearly an order of magnitude faster so that a broad range of parameter space could be examined. Second, only models that reproduced the observed electron temperature will be valid, so this decouples the ionization and thermal parts of the problem during this early stage of the solution. The balance between heating and cooling determines the electron temperature. Some of the dominant heating agents (for instance, grain photoionization and the associated question of the grain abundance) are not well constrained by our observational database. Abundances of these constituents will be fitted later.

A plane-parallel closed geometry was assumed. The plane-parallel assumption is appropriate when the thickness of the shell is considerably smaller than the radius. A closed or symmetric geometry is one in which diffuse radiation from one side of the shell crosses the central hole and strikes the far side of the cloud, as would be the case if the shell nearly fully covers the continuum source. The images suggest that these are indeed the case.

We assumed a microturbulence of 5 km s^{-1} to simulate the effects of the observed range of velocities. This is important because it has the effect of diminishing hydrogen Lyman line opacity and increases the deviations from Case B.

The fitting was done in terms of the ionization parameter U, the dimensionless ratio of the flux density of hydrogen-ionizing photons to hydrogen at the illuminated face of the cloud defined as

$$U \equiv \frac{\Phi({\rm H})}{n_e c} , \quad (11)$$

where Φ(H) is the surface flux of ionizing photons (cm^{-2} s^{-1}). The ionization parameter is the quantity that directly determines the level of ionization of the gas. The deduced electron density places this nebula well within the low-density limit, so the density has no direct effect on the spectrum, except through changes in U. Working in terms of U combines the two unknowns Φ(H) and n_e into the single parameter that determines the observed spectrum. This simplifies the analysis significantly.

The density and thickness of the cloud were kept constant at the values deduced above. Together these automatically reproduce the observed surface brightness of the cloud. That surface brightness could be reproduced for other values of the density, were the thickness to be adjusted properly. The density/thickness pair of parameters has no effect on the spectrum other than reproducing the observed surface brightness, so there is no profit in varying these strongly coupled parameters.

No significant problems were encountered in fitting the spectrum. Table 3 presents the results at this stage. The deduced parameters are He/H = 0.094, C/H = 1.7×10^{-4}, O/H = 3.9×10^{-4}, N/H = 6.9×10^{-5}, Ne/H = 6.5×10^{-5}, S/H = 5.2×10^{-6}, Ar/H = 5.8×10^{-7}, log $U = -2.55$, and $T_* = 1.50 \times 10^5$ K. The abundances are typically about half-solar but well within the range of observed abundances for PNs. The central star temperature is higher than that obtained from observations of the photospheric lines, and the nebular helium abundance is about two-thirds of that derived from the central star atmosphere models (He/H = 0.14 ± 0.03 was found by Napiwotski 1999).

One surprising result of this simple analysis is that it is clear that estimates of the ionization correction factor (ICF) for oxygen, based on the observed ionization of helium, would not work well for this object. Alexander & Balick (1997) have shown that the ICF method generally does work in radiation-bounded nebulae. In this model (and later ones too) most of the helium is fully ionized, with only about 9% of He in the form of He^+. Ionization potentials would suggest that this would also be the ratio of O^{++}/O. Actually, the O^{++}/O ionic fraction is nearer 30%, so an ICF-approached abundance analysis would overestimate the oxygen abundance by roughly a factor of 3. In a fully ionized nebula such as A39, the role played by the detailed atomic physics is exaggerated, while in a radiation-bounded nebula photon, counting becomes more important and ionization potential based arguments work better. Consequently, a much improved abundance measurement is obtained using the modified ICF approach suggested first by Kingsburgh & Barlow (1994) and incorporated by Alexander & Balick (1997) wherein the ICFs are adjusted according to fits to photoionization models.

5.2. *Achieving Thermal Equilibrium*

At this stage the constant electron temperature assumption has produced good agreement with the spectrum. The next step is to achieve this electron temperature in a thermal equilibrium model. The balance between heating and cooling sets the electron temperature. For the model listed in Table 3 the integrated heating is 95% of the cooling. This model is not in thermal equilibrium.

A set of thermal equilibrium calculations was performed that used the derived parameters of the constant temperature calculation as a starting point. The abundances, stellar temperature, and the ionization parameter were varied, but the dust-to-gas ratio, important because of the effects of photoelectric heating of grains, was left at its default (Kingdon & Ferland 1997). The results and parameters are listed in Tables 3 and 4.

We took two approaches in the final optimization. First, we held the stellar temperature fixed at 115,000 K, the value deduced from photospheric lines. This largely reproduces the overall spectrum but does not reproduce the strong oxygen lines to the expected precision. The [O III] lines are major coolants, so if they are not correct, then the overall thermal equilibrium is not correct.

In the second approach, we allowed the stellar temperature to vary also and obtained somewhat better results. The deduced stellar temperature is somewhat higher than that deduced from the photospheric lines. This difference is most likely an artifact of the model stellar atmospheres that are assumed. Our approach matches the predicted ionizing continuum to that needed to produce the observed ionization. At the time of this writing, a second generation of Rauch atmospheres is under construction. The grids are not yet extensive enough to use in our modeling, but we are able to compare the new results, which include opacities of iron peak elements, with those we use here. The continua in the Wien tail, the part responsible for photoionization of higher ionization potential species, differ by factors of 0.5–1 dex with the new atmospheres producing the fainter continua.

TABLE 3

LINE RATIO RESULTS FROM CLOUDY OPTIMIZATIONS

ID	λ	Observed	Error	Constant Temperature	Thermal 1	Thermal 2
H I + He II.....	4861	1.00		1.00	1.00	1.00
He II	4686	0.96	0.05	0.917	0.99	0.941
He I.....	5876	0.02	0.40	0.010	0.025	0.011
[O III]	5007	11.31	0.05	11.30	11.9	11.5
[O III]	4363	0.24	0.09	0.244	0.242	0.261
[O II]	3727	0.40	0.15	0.406	0.245	0.479
[Ne III]	3869	1.04	0.15	1.10	1.50	0.992
[Ne IV]	4720	0.01	0.20	0.015	0.008	0.014
C IV	1549	7.30	0.06	7.41	6.84	7.41
[S II].....	6725	0.04	0.20	0.047	0.081	0.10
[S III]	9069	0.18	0.40	0.261	0.277	0.210
[Ar III]	7135	0.06	0.30	0.064	0.0815	0.085
[Ar IV]	4740	0.04	0.30	0.025	0.0322	0.0305

NOTE.—The columns marked "Observed" and "Error" give the observed intensities and associated uncertainty expressed as a fractional error. The next column gives the predicted line ratios from the constant temperature model. The last two columns give results for the thermal equilibrium models. In the first (marked "Thermal 1") the stellar temperature was held fixed at 115,000 K, the temperature deduced from the photospheric lines, and in the second (marked "Thermal 2") the stellar temperature was allowed to vary.

TABLE 4

DEDUCED PARAMETERS[a]

Parameter	Constant Temperature	Thermal Equilibrium 1	Thermal Equilibrium 2	Typical PN[b]	Solar[c]
log U	−2.55	−2.425	−2.60	...	...
T_* (K).....	1.50×10^5	1.15×10^5	1.52×10^5	...	...
He/H	−1.025	−0.962	−0.992	−0.939	−1.009
C/H	−3.76	−3.82	−3.81	−3.26	−3.40
N/H	−4.16	−3.74	−4.19	−3.86	−4.00
O/H	−3.41	−3.64	−3.46	−3.32	−3.07
Ne/H	−4.18	−4.31	−4.28	−3.91	−3.91
S/H	−5.29	−5.27	−5.42	−5.08	−4.79
Ar/H	−6.24	−6.18	−6.16	−5.61	−5.44

[a] Abundance values are given as logs by number relative to hydrogen. Model "Thermal Equilibrium 1" held the stellar temperature fixed at 115,000 K, while the second allowed the stellar temperature to vary.

[b] From Kingsburgh & Barlow 1994 for non–type I PNs.

[c] From Grevesse & Anders 1989; Grevesse et al. 1990, 1991.

Given this uncertainty in the model stellar continua, we do not feel that there is any conflict between our results and previous work.

6. DISCUSSION

6.1. *The Presence of* Ne V

Simply by its presence, the [Ne V] line implies a very high temperature for the central star and a very high excitation nebula. This line was not included in the modeling done above, although the line is detected with considerable certainty. But is the line real? After very close scrutiny, we can report the following facts that raise some suspicion. The line has a spatial extent that exceeds any other line in the spectrum. It exhibits a surface brightness distribution along the slit that is more or less uniform, whereas the other lines peak strongly across the bright rim of the nebula. If the line is present, the temperature of the exciting star must be higher than the atmospheric model results (Napitwotzki 1999; McCarthy et al. 1997) or deduced in the photoionization analysis by 10,000–30,000 K in order to ionize the gas to Ne^{+4}.

Although we are concerned about the reality of the [Ne V] feature, we believe that it is real for the following reasons. First, its wavelength is within 0.5 Å of that expected for the velocity of the nebula and well within the uncertainty of the wavelength solution (~1 Å) in this part of the spectrum. Second, the line is visibly present in several exposures, although quite weak in all. Third, it has an extent that is centered on the nebula, while being clearly different than the full slit profile that arises from a line in the sky. Fourth, it has a spectral resolution consistent with a genuine emission line. (Fig. 4 illustrates the spectral region around the [Ne V] line. The apparent line to the left is a residual cosmic-ray event that proved robust to the rejection algorithm.) Fifth, we see evidence for enhanced levels of ionization at the periphery of the nebula that suggest the presence of an outer, low-density halo (see § 3.1) of very high ionization.

Figure 8 shows several line ratios of interest as a function of position along the slit. The rise in line ratios at the outer edges of the slit indicates that the excitation of the nebula increases beyond the outer rim that is defined by the [O III] image. Note that the ratio of [O III] λ4959 to Hβ rises as the intensity of Hβ begins to drop beyond the rim, while the ratio of He^{++} λ4686 to Hβ remains more constant. Since helium is almost completely doubly ionized throughout the nebula, it cannot increase much further. The ionization stages of oxygen, on the other hand, can continue to rise.

The existence of a very high ionization outer halo may be an important component for other fully ionized nebulae, adding to their total masses. In order to assess the possible extent of such a halo, R. Reynolds (Univ. Wisconsin) kindly examined his extremely deep Hα images of this region taken with the WHAM survey camera on Kitt Peak (Haffner, Reynolds, & Tufte 2000). He reports that there is no evidence for a giant ionized halo around A39, down to a surface brightness level of 5×10^{-18} ergs cm^{-2} s^{-1} $arcsec^{-2}$, averaged over the WHAM resolution element of 1°. This is the level of the diffuse Galactic emission in this direction, and so a fainter halo may exist but be lost in the diffuse emission, or a smaller halo could exist and probably does based on the spectroscopic evidence.

The excitation of this outer gas is consistent with photoionization of a very low density shell by the continuum that

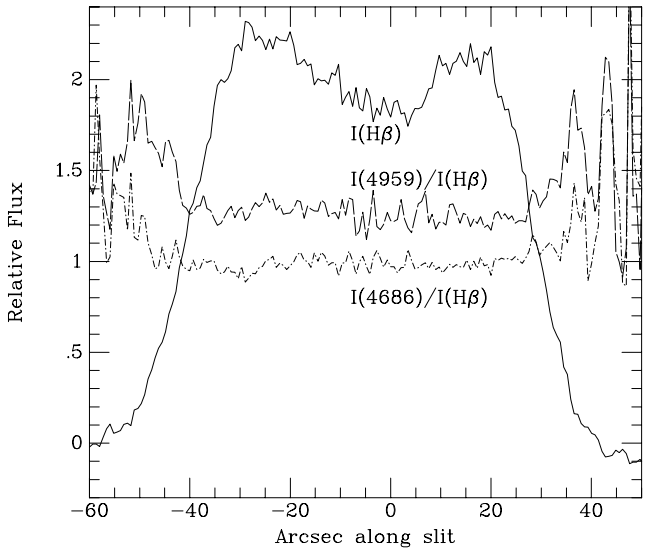

FIG. 8.—Strength of Hβ and the relative ratios of [O III]/Hβ and He II/Hβ are shown as a function of position along the slit. Beyond the two peaks as the slit crosses the bright rim of the nebula, the excitation level continues to increase outward into the nebula halo. The spectrum becomes too noisy to provide any useful excitation information beyond the positions shown.

filters through the main shell. The density in the outer shell must be considerably lower than the density of the main shell since its surface brightness is so low. Estimating that the Hβ surface brightness in the outer shell is $\sim$10 times smaller than the main shell, the corresponding density is $\sim$3 times smaller if the thickness of main and outer shells is the same, and even smaller if the thickness of the outer shell is larger than the main shell. The main shell is optically thin to ionizing radiation, which accounts for its low surface brightness, so this (slightly) filtered light passes through the main shell and strikes the lower density outer region. The level of ionization of the gas is proportional to both the stellar temperature and the ionization parameter. Although the continua striking both shells are essentially the same, the outer shell will have an ionization parameter more than 0.5 dex larger than the main shell as a result of its low density. This results in higher ionization and is the most likely explanation for the [Ne v] line. The present data set does not provide enough constraints to justify creating a model for the outer region.

6.2. *The Mass of A39*

The mass adopted for the shell, 0.6 $M_\odot$, is reasonable for a fully ionized PN. When we add up the total mass of the system, 0.6 $M_\odot$ in the nebula and 0.61 $M_\odot$ in the central star, the progenitor would have been 1.2 $M_\odot$. The implied progenitor mass that produces a central star of 0.61 $M_\odot$ is $\sim$2.1 $M_\odot$, which is significantly larger than the inferred mass budget for the descendents. If the stellar temperature is truly as low as Napiwotzki (1999) and McCarthy et al. (1997) suggest ($\sim$117,000 K), then the mass budgets are more consistent. However, that temperature is inadequate to drive the [Ne v] line to a visible level. Either the line is an artifact (but see § 6.1), or the initial to final mass relations are not sufficiently accurate, or the mass budget of the nebula plus star does not fully account for lost material (e.g., dust mass, gas lost during the red giant branch phase).

6.3. *Central Star Positional Offset*

We noted in § 3.5 that the central star is offset 2″ to the west of the center of the circle defined by the nebular rim. Usually, a stellar offset is associated with an ISM interaction in which the star catches up with the impeded leading edge of the nebula. In this case, the star appears to be closer to the trailing edge of the nebula because the star is closer to the low surface brightness western half of the nebula.

Instead, we propose that the offset of the star may have been induced by a nonsymmetric mass-loss episode that favored mass loss to the east. If so, then we can explain, in part, the brighter eastern rim as a consequence of higher density arising from the slightly asymmetric ejection process rather than the more conventional explanation of an interaction with the ISM. We also can explain the wrong-way central star positional offset. Through conservation of momentum, a differential mass loss of $\sim$0.05 $M_\odot$ is sufficient to accelerate the central star to the required speed of 0.9 km s^{-1}.

If there is a large central star motion along the line of sight in addition to the small implied tangential velocity of 0.9 km s^{-1}, then another explanation may be required. The referee pointed out to us that the Hα emission seen in Figure 4 of Napiwotzki (1999) suggests that the central star of A39 may have a significant redshift of $\sim$40 km s^{-1} relative to the nebula. R. Napiwotzki (2001, private communication) kindly provided us with his spectra for evaluation of this point, as well as his interpretation of the apparent redshift. Because he applied a careful sky-plus-nebula subtraction for the figure in Napiwotzki (1999), the emission shown is likely stellar in origin, suggesting a wind from the star rather than a nebular velocity offset. Thus, the existence of a significant velocity difference between the star and the nebula remains an open question.

6.4. *Success of the Photoionization Model*

Overall, the nebular spectrum is modeled very well. Tests show that the sizes of the differences between the final model and the observations were about the same level as would be produced by using slightly different stellar atmospheres. (Tests were done with solar and halo abundance Rauch models, with several surface gravities, and also the earlier Werner models.) Trying to match these lines any better would mainly become a test of the stellar atmosphere models.

In particular, we note that our value of $T_{\rm eff}$ (150,000 K) is somewhat higher than the value of 117,000 $\pm$ 11,000 K derived by Napiwotzki (1999). As noted in § 5.2, models at lower temperatures failed to reproduce reasonable values for the well-observed oxygen line ratios, such as I(3727)/I(5007), and they produced no emission of [Ne v]. On the other hand, our model at 150,000 K, in which the [Ne v] line was not used as a constraint, produces too much [Ne v] by a factor of 4. We attempted a third model, where we allowed the stellar temperature to vary but constrained the [Ne v] to be close to the observed value; the derived temperature then drops to 130,500 K, but again, the oxygen ratios are too low. Much of the problem with modeling these lines is related to the great uncertainty of the stellar atmospheres and the consequent emerging ionizing flux. Because this area is still developing, we do not consider the different values of temperature to be a significant problem in the photoionization models but rather evidence for more work needed in the field of hot star atmospheres.

We did not encounter any further constraints that were difficult to meet largely because the nebula's low surface brightness and resulting modest spectral signal-to-noise ratio prevented us from detecting many lines. In part, this is a disappointment; for this fully ionized nebula, the special geometry is not a significant advantage in relieving model constraints because other geometries would suffice. Nevertheless, we provide a list of predicted line strengths relative to Hβ in Tables 5 and 6 for which future observers with deeper spectra can test our model. It is likely that future instrumentation will be able to detect some of the C or O recombination lines that provided our original motivation. Table 5 contains the more common emission lines, down to a strength of 1% of Hβ. Table 6 pushes the predicted line list below 0.1% of Hβ but is restricted to the recombination lines of CNO in order to keep the list manageable.

We caution other PN researchers that the hydrogen spectrum in this sort of nebula is not precisely case B (Table 5). Collisional excitation of Hα and escape of Lyman lines are both important, with the effect that the Hα/Hβ ratio is predicted to be 2.92 while the case B value is 2.78. Note again that helium is a significant contributor to the emission at λ4861 and must be accounted as was done in Table 5.

We further caution users of ICF methods for abundance determinations that oxygen abundances can be wrong by

TABLE 5

PREDICTED MODEL LINE RATIOS[a]

Ion	λ	$I/I(H\beta)$ Thermal 1	$I/I(H\beta)$ Thermal 2	Ion	λ	$I/I(H\beta)$ Thermal 1	$I/I(H\beta)$ Thermal 2
H I	973	0.1873	0.0992	Si II.....	2335	0.0139	0.0261
C III	977	0.7849	0.6744	Ne IV.....	2424	0.7404	0.014
N III	990	0.4262	0.1542	Ne V	3346		0.104
H I	1026	0.2172	0.1309	Ne V	3426		0.285
He II.....	1085	1.0332	0.9902	S III.....	3722	0.0242	0.0194
N II.....	1085	0.0327	0.0115	O II.....	3727	0.2445	0.4785
C III	1176	0.0257	0.0218	Ne III.....	3869	1.4952	0.9922
S III.....	1194	0.0122	0.0103	Fe V.....	3892	0.0308	0.0237
Si III	1207	0.1884	0.2491	Ne III.....	3968	0.4506	0.299
He II.....	1215	2.2394	2.1436	H I	4340	0.448	0.4456
H I	1216	27.5775	33.6762	O III.....	4363	0.2417	0.2612
N V.....	1239	0.055	0.1042	He II	4687	0.992	0.9406
N V.....	1243	0.0296	0.0544	Ar IV	4711	0.0426	0.0402
Si II.....	1260	0.017	0.0192	Ne IV.....	4720	0.0081	0.0140
C II	1335	0.0785	0.0965	Ar IV	4740	0.0322	0.0305
Si IV	1394	0.2983	0.3115	H I	4861	0.949	0.951
O IV	1397	0.0164	0.0353	He II	4861	0.051	0.049
O IV	1400	0.0481	0.1033	O III.....	4959	3.9232	3.8144
O IV	1401	0.0959	0.206	O III.....	5007	11.8089	11.4814
Si IV	1403	0.1587	0.1629	He I	5876	0.0251	0.0111
O IV	1405	0.1252	0.2688	S III.....	6312	0.041	0.0329
O IV	1407	0.0466	0.0999	N II.....	6548	0.0648	0.0421
S IV	1417	0.018	0.0142	H I	6565	2.7181	2.7926
N IV	1485	1.027	0.4072	He II	6562	0.135	0.1279
C IV	1548	4.5359	4.9195	N II.....	6584	0.1913	0.1242
C IV	1551	2.303	2.4936	S II	6716	0.0467	0.0578
He II.....	1640	7.0223	6.6835	S II	6731	0.0343	0.0426
O III	1661	0.178	0.1985	Ar V.....	7005		0.011
O III	1666	0.4387	0.4893	Ar III	7135	0.0815	0.0848
S III.....	1720	0.0288	0.0259	O II.....	7325		0.0167
N III	1747	0.049	0.0191	Ar III	7751	0.0197	0.0205
N III	1749	0.1727	0.0674	S III.....	9069	0.2774	0.2103
N III	1751	0.3783	0.1475	S III.....	9532	0.6879	0.5215
N III	1752	0.477	0.1861	S IV	10.5	1.477	
N III	1754	0.1738	0.0678	Ne V	14.3		0.745
Si II.....	1808	0.045	0.0883	Ne III.....	15.6	0.612	0.372
Si III	1883	0.8615	1.1185	S III.....	18.7	0.212	0.155
Si III	1892	0.5088	0.6605	Ne V	24.3		0.827
C III	1907	2.7903	3.0901	O IV.....	25.9	7.64	12.8
C III	1910	1.8106	2.0052	S III.....	33.5	0.429	0.312
O III	2321	0.0558	0.0589	Si II.....	34.8	0.051	0.0817
C II	2325	0.012	0.0215	Ne III.....	36	0.055	0.0333
C II	2327	0.0524	0.0935	O III.....	51.8	1.05	0.942
C II	2328	0.0383	0.0687	N III.....	57.2	1.69	0.545
C II	2329	0.0125	0.0224	O III.....	88.4	1.57	1.42

NOTE.—Wavelengths are given in Å, except for the reddest lines, which have wavelengths less than 100: these are in μm. Table 5 is also available in machine-readable form in the electronic edition of the *Astrophysical Journal*.

[a] For silicon, where no lines were observed, we assume $Si/H = 10^{-5}$.

factors of several in fully ionized nebulae. This matter-bounded shell would correspond to only a tiny portion of the structure of a radiation-bounded nebula. The ICF methods work for the radiation-bounded case in which all ionizing photons are absorbed so that photon counting and ionization potential arguments work. In the matter-bounded case we sample what would be a small piece of the radiation-bounded case, and the ionization distribution is linearly affected by recombination coefficients and photoionization cross sections.

7. CONCLUSIONS

The PN A39 is a beautiful example of what a PN is supposed to look like: a nearly perfect limb-brightened circular shell with an obvious central star. Its special geometry would allow a test of various photoionization models if our spectra had gone deep enough to provide tighter constraints. Future observers may be able to test our model predictions and take advantage of the unique spherical geometry.

Although we were able to reproduce the line ratios without excessive challenge, this apparently very simple nebula provided plenty of surprises to consider:

1. Galactic PN distances are always a problem. The Shklovskii distance disagrees only slightly with the

TABLE 6

WEAK CNO RECOMBINATION LINES

Ion	λ	$I/I(\mathrm{H}\beta)$ Thermal 1	$I/I(\mathrm{H}\beta)$ Thermal 2	Ion	λ	$I/I(\mathrm{H}\beta)$ Thermal 1	$I/I(\mathrm{H}\beta)$ Thermal 2	Ion	λ	$I/I(\mathrm{H}\beta)$ Thermal 1	$I/I(\mathrm{H}\beta)$ Thermal 2
O V	141	0.0000	0.0011	N III.....	374	0.0794	0.0258	C II.....	1093	0.0037	0.0034
O IV.....	159	0.0125	0.1567	O IV.....	380	0.0010	0.0132	C II.....	1168	0.0009	0.0008
O V	168	0.0000	0.0010	O II	386	0.0094	0.0082	O IV.....	1213	0.0002	0.0028
O IV.....	171	0.0011	0.0133	O II	386	0.0139	0.0121	C III	1247	0.0061	0.0052
N IV.....	178	0.0018	0.0030	N III.....	387	0.0794	0.0249	O IV.....	1289	0.0004	0.0046
O IV.....	183	0.0017	0.0208	N III.....	391	0.0455	0.0149	C III	1296	0.0017	0.0015
O IV.....	184	0.0010	0.0148	C III	398	0.0409	0.0342	N IV.....	1325	0.0005	0.0010
O IV.....	188	0.0032	0.0446	N III.....	411	0.0187	0.0059	O IV.....	1342	0.0008	0.0105
O V	193	0.0000	0.0012	C III	412	0.0632	0.0530	N II	1345	0.0013	0.0004
O IV.....	196	0.0147	0.1889	N III.....	419	0.0677	0.0213	C III	1478	0.0015	0.0013
O IV.....	201	0.0227	0.2795	C III	433	0.0044	0.0037	C III	1491	0.0014	0.0012
O IV.....	203	0.0013	0.0161	O IV.....	443	0.0001	0.0017	N III.....	1498	0.0043	0.0013
O IV.....	207	0.0033	0.0419	C III	451	0.0047	0.0040	C III	1549	0.0011	0.0009
O IV.....	211	0.0032	0.0418	C III	460	0.0743	0.0633	C III	1577	0.0157	0.0132
O IV.....	213	0.0027	0.0338	N III.....	472	0.0181	0.0057	N IV.....	1719	0.0011	0.0020
O IV.....	216	0.0009	0.0115	C III	476	0.0101	0.0086	N II	1742	0.0039	0.0012
N IV.....	218	0.0022	0.0038	C III	484	0.0067	0.0057	C III	1797	0.0010	0.0008
N IV.....	222	0.0010	0.0016	O IV.....	487	0.0003	0.0040	C III	1828	0.0134	0.0112
O IV.....	224	0.0052	0.0639	C III	493	0.0066	0.0056	N III.....	1857	0.0013	0.0004
N IV.....	225	0.0053	0.0090	C III	494	0.0097	0.0082	N III.....	1885	0.0067	0.0021
N IV.....	234	0.0006	0.0010	C III	512	0.0047	0.0040	C III	1923	0.0009	0.0008
O IV.....	239	0.0020	0.0252	C III	538	0.0057	0.0050	C III	1923	0.0062	0.0053
N IV.....	240	0.0028	0.0047	O III.....	542	0.0239	0.0397	O III.....	1924	0.0014	0.0023
O IV.....	250	0.0034	0.0459	O IV.....	554	0.0079	0.1014	O III.....	1947	0.0029	0.0049
O IV.....	253	0.0030	0.0406	C III	574	0.0050	0.0043	C III	2017	0.0022	0.0019
O IV.....	259	0.0021	0.0278	O III.....	600	0.0245	0.0417	N III.....	2064	0.0130	0.0041
O IV.....	261	0.0069	0.0882	O IV.....	609	0.0034	0.0444	O III.....	2092	0.0018	0.0029
O IV.....	266	0.0140	0.1770	O IV.....	617	0.0030	0.0403	C III	2114	0.0010	0.0009
O IV.....	267	0.0021	0.0275	O IV.....	637	0.0005	0.0057	C III	2163	0.0009	0.0008
O IV.....	274	0.0024	0.0333	N II	646	0.0168	0.0053	N III.....	2188	0.0049	0.0015
O IV.....	276	0.0025	0.0338	N III.....	686	0.0484	0.0157	C III	2200	0.0013	0.0011
O IV.....	280	0.0007	0.0094	O III.....	703	0.0768	0.1304	C III	2296	0.0009	0.0008
N IV.....	284	0.0057	0.0099	O IV.....	704	0.0004	0.0044	C III	2297	0.0164	0.0139
O IV.....	286	0.0015	0.0198	O IV.....	713	0.0008	0.0107	O IV.....	2450	0.0003	0.0040
O IV.....	289	0.0021	0.0266	N IV.....	716	0.0006	0.0010	O IV.....	2511	0.0002	0.0021
O IV.....	290	0.0005	0.0063	O IV.....	746	0.0003	0.0033	C III	2512	0.0013	0.0011
N IV.....	298	0.0012	0.0020	N III.....	764	0.0730	0.0233	C IV	2529	0.0010	0.0021
O III.....	299	0.0897	0.1499	O IV.....	780	0.0076	0.0988	O IV.....	2620	0.0001	0.0012
O III.....	301	0.2190	0.3643	N III.....	783	0.0294	0.0094	O IV.....	2638	0.0001	0.0009
O IV.....	304	0.0001	0.0019	C II.....	800	0.0559	0.0503	O IV.....	3038	0.0001	0.0018
O IV.....	307	0.0006	0.0080	O IV.....	844	0.0011	0.0143	O III.....	3265	0.0054	0.0090
N III.....	312	0.0230	0.0073	N II	916	0.0103	0.0034	O III.....	3762	0.0031	0.0052
O III.....	321	0.0530	0.0886	O IV.....	923	0.0009	0.0123	C III	4069	0.0014	0.0012
N III.....	323	0.0788	0.0267	N IV.....	923	0.0019	0.0032	N III.....	4379	0.0019	0.0006
N IV.....	323	0.0011	0.0019	C II.....	946	0.0080	0.0072	O IV.....	4632	0.0001	0.0014
N III.....	340	0.1824	0.0584	N III.....	980	0.0037	0.0012	C III	4649	0.0013	0.0012
O IV.....	342	0.0001	0.0009	N IV.....	1036	0.0011	0.0018				
N III.....	349	0.2916	0.0909	C II.....	1037	0.0115	0.0108				
C III	372	0.0101	0.0087	O IV.....	1046	0.0001	0.0013				
O III.....	374	0.0537	0.0902	O IV.....	1068	0.0005	0.0069				

NOTE.—Table 6 is also available in machine-readable form in the electronic edition of the *Astrophysical Journal*.

spectroscopic distance, but we must assume a nebular mass that is at the high end of the nebular mass distribution.

2. The presence of [Ne V] just outside the main nebula implies an unusual ionization structure, with a large low-density extended halo. The high ionization is likely the result of the low density and resulting high-ionization parameter.

3. The "central" star is offset from the nebular center by 2″. The offset does not appear to be a consequence of an interaction with the ISM. We speculate that a small asymmetric mass ejection has accelerated the star.

4. The nebula is close to, but not exactly, a uniform spherical shell. The east rim of the nebula is 50% brighter than the west rim, and irregularities in the surface brightness are evident across the face of the shell. The cause of the east-west dichotomy is not known but could be related to the offset of the central star.

5. The oxygen abundance was determined to be 3 times smaller than the ICF method would predict. This discrepancy is unexpectedly high and represents the typical uncertainty in the method when applied to a fully ionized nebula.

6. The very low surface brightness made it impossible to

detect the faint emission lines that were the original motivation for this investigation. We provide a list of predicted emission lines to encourage future work.

We wish to thank Daryl Willmarth and Di Harmer for obtaining the extraordinary images of A39 for us at the WIYN telescope and R. Reynolds for providing details about the WHAM survey. R. Napitwotzki kindly provided us with the spectra of A39 used for his 1999 paper in order to check for a velocity offset between the central star and the nebula. We are grateful to the anonymous referee for a very careful reading of the original manuscript and several valuable suggestions that greatly improved the content of this paper. This work was supported by STScI with grant GO-07284.01-96A. Research in Nebular Astrophysics in Lexington is supported by the NSF and NASA through grants AST 0071180 and NAG5-8212.

REFERENCES

Abell, G. O. 1966, ApJ, 144, 259
Alexander, J., & Balick, B. 1997, AJ, 114, 713
Ali, B., Blum, R. D., Bumgardner, T. E., Cranmer, S. R., Ferland, G. J., Haefner, R. I., & Tiede, G. P. 1991, PASP, 103, 1182
Bergeron, P., Wesemael, F., & Beauchamp, A. 1995, PASP, 107, 1047
Cardelli, J. A., Clayton, G. C., & Mathis, J. S. 1989, ApJ, 345, 245
Claver, C. F., Liebert, J., Bergeron, P., & Koester, D. 2001, ApJ, in press
Ferland, G. J. 1999, PASP, 111, 1524
———. 2001a, PASP, 113, 41
———. 2001b, Hazy, A Brief Introduction to CLOUDY, Univ. Kentucky Internal Rep.
Garnett, D. H., & Dinerstein, H. L. 2001, ApJ, in press
Grevesse, N., & Anders, E. 1989, in AIP Conf. Proc. 183, Cosmic Abundances of Matter, ed. C. J. Waddington (AIP: New York), 1
Grevesse, N., Lambert, D. L., Sauval, A. J., van Dishoeck, E. F., Farmer, C. B., & Norton, R. H. 1990, A&A, 232, 225
———. 1991, A&A, 242, 488
Haffner, L. M., Reyonolds, R. I., & Tufte, S. L. 2000, Rev. Mexicana Astron. Astrofis., 9, 238
Hippelein, H., & Weinberger, R. 1990, A&A, 232, 129
Kaler, J. B. 1983, ApJ, 271, 188
Kingdon, J. B., & Ferland, G. J. 1997, ApJ, 477, 732
Kingsburgh, R. L., & Barlow, M. J. 1994, MNRAS, 271, 257
Liu, X.-W. 1998, MNRAS, 295, 699
Mathis, J. S., Torres-Peimbert, S., & Peimbert, M. 1998, ApJ, 495, 328
McCarthy, J. K., Méndez, R. H., & Kudritzki, R.-P. 1997, in IAU Symp. 180, Planetary Nebulae, ed. H. J. Habing & H. J. G. L. M. Lamers (Dordrecht: Kluwer), 120
Napiwotzki, R. 1999, A&A, 350, 101
Napiwotzki, R., & Schönberner, D. 1995, A&A, 301, 545
Nussbaumer, H., & Storey, P. J. 1987, A&AS, 69, 123
Osterbrock, D. E. 1989, in Astrophysics of Gaseous Nebulae and Active Galactic Nuclei (Mill Valley: University Science), 17
Pagel, B. E. J. 1997, Nucleosynthesis and Chemical Evolution of Galaxies (Cambridge: Cambridge Univ. Press)
Phillips, J. P., & Pottasch, S. R. 1984, A&A, 130, 91
Pottasch, S. R. 1984, Planetary Nebulae: A Study of Late Stages of Stellar Evolution (Dordrecht: Reidel)
Rauch, T. 1997, A&A, 320, 237
Richer, H. B., et al. 1997, ApJ, 484, 741
Savin, D. W. 2000, ApJ, 533, 106
Savin, D. W., et al. 1999, ApJS, 123, 687
Schlegel, D. J., Finkbeiner, D. P., & Davis, M. 1998, ApJ, 500, 525
Stasinska, G., Gorny, S. K., & Tylenda, R. 1997, A&A, 327, 736
Storey, P. J., & Hummer, D. G. 1995, MNRAS, 272, 41
Tweedy, R. W., & Kwitter, K. B. 1996, ApJS, 107, 255
Tylenda, R., Acker, A., Raytchev, B., Stenholm, B., & Gleizes, F. 1991, A&AS, 89, 77
Weidemann, V. 2000, A&A, 363, 647
Williams, R. E. 1992, ApJ, 392, 99